CrossMark

ORIGINAL PAPER

Development of MgO–Y$_2$O$_3$ Composite Nanopowder by Pechini Sol–Gel Method: Effect of Synthesis Parameters on Morphology, Particle Size, and Phase Distribution

S. Ghorbani[1] · R. Sh. Razavi[1] · M. R. Loghman-Estarki[1] ·
A. Alhaji[1]

Abstract MgO–Y$_2$O$_3$ composite nanopowder was synthesized from Pechini method. Several experiments were conducted to examine the effects of the molar ratio of citric acid (CA) to transition metals (TM) calcination temperature and the pH value on the morphology, phases, and specific surface area of the samples. As-synthesized MgO–Y$_2$O$_3$ composite nanopowder were characterized by X-ray diffraction, field-emission scanning electron microscope (FESEM), transmission electron microscope, BET, thermal gravimetric–differential thermal analysis and Fourier transform infrared analysis. FESEM analysis revealed that the sample with the pH value of 1 and CA:TM = 10:1, had good homogeneity, and a spherical morphology with the particle size of 19.5 nm, while by increasing the pH up to 7 and 12, the particle size increased to 28.5 and 30.9 nm respectively. By increasing the mole ratio of CA to TM, the particle size and the specific surface area of MgO–Y$_2$O$_3$ composite nanopowder has reduced and by increasing the pH from 1 to 7 and 12, the particle size and the specific surface area of MgO–Y$_2$O$_3$ composite nanopowder has increased.

Keywords Magnesia · Yttria · Nanocomposite · Sol–Gel

Introduction

Y$_2$O$_3$ and MgO have excellent optical properties in the visible and infrared range. Meanwhile, mechanical and thermal shock resistance properties are required for IR windows and domes applications [1–3]. MgO–Y$_2$O$_3$ nanocomposite with cubic

✉ S. Ghorbani
    sghorbani1375@gmail.com

[1] Department of Materials Engineering, Malek Ashtar University of Technology,
     P.O. Box 83145/115, Shahin Shahr, Isfahan, Iran

structure is one of the most important transparent ceramics owing to its good combination of grate mechanical and optical properties [4–9] that MgO–Y$_2$O$_3$ composites have good properties such as, 80% IR transmittance at 6 μm wavelength, and a 40% increase in biaxial flexural strength compared with pure Y$_2$O$_3$ [9–11]. With the development of nanotechnologies and fabrication techniques of transparent ceramics, polycrystalline MgO–Y$_2$O$_3$ nanocomposite transparent ceramics have attracted considerable attention due to its excellent thermo-mechanical properties [12–14]. Synthesis of nanopowders with a small grain size and a spherical morphology is a prerequisite for enhancing emission intensity and other properties. The chemical methods such as hydrothermal precipitation, co-precipitation and sol–gel techniques offer fine ceramic powders [13–15]. Wet chemical method, the sol–gel route, utilize lower temperatures and offer a greater degree of control over elemental ratios and homogeneity [16–18]. Sol–gel procedures are well suited for the production of ceramics as they offer good control over grain size, composition, and microstructural homogeneity at the atomic scale, using lower processing temperatures. The main disadvantage is that alkoxide-based sol–gel processing needs precise control of synthesis situations and costly organometallic transition metals [19, 20]. Thus, alkoxide sol–gel processed MgO–Y$_2$O$_3$ nanocomposite can be costly. The coast effective derivative of the sol–gel technique is Pechini sol–gel method. This technique, due to the suitable cost and facility and low calcination temperature is considered. Ethylene glycol (EG) addition led to increasing the polymerization (esterification). After polymerization the high chelating between CA and cations molecule occurs [20–34]. Oghaz and coworkers prepared ceria–yttria co-stabilized zirconia (CYSZ) nanoparticles by sol–gel process. They synthesized ceria–yttria co-stabilized zirconia (CYSZ) nanoparticles with an average particle size of 25 nm [16]. Chun-Hu Chen and coworkers prepared Magnesia–Yttria composites nanopowder by the esterification sol–gel route method [32]. Thy synthesized Magnesia–Yttria composites nanopowders with extremely fine, uniform grains, and phase domains by the CA:TM: 1:1 mol ratio [32]. In another study, Shengquan Xu and entourage synthesized MgO–Y$_2$O$_3$ composites nanopowder using the sol–gel Combustion method. They studied the effect of mole ratio of yttrium nitrate to the whole precursor mixture and the holding temperature on the properties of the composite nanopowder. When the ratio of yttrium nitrate to the whole precursor mixture reaches 22.5 mol%, the average particle size of synthesized composite nanopowder is 13 nm and the specific surface area is 45.9 m^2/g [33]. In another study by S. Ghorbani and coworkers, synthesized MgO–Y$_2$O$_3$ composites nanopowders. They synthesized MgO–Y$_2$O$_3$ composites nanopowders with an average grain size of 30 nm by sol–gel method [34]. According to these studies, sol–gel Pechini is a good method for preparing nanopowders with a spherical morphology, low agglomeration, and a small grain size.

In this paper, we have developed MgO–Y$_2$O$_3$ composites nanopowder using the polyester based sol–gel route and the influence of pH value and CA content on the morphology, particle size and phase distribution of MgO–Y$_2$O$_3$ composite nanopowders studied using FESEM, TEM, XRD, TG–DTA, BET, ICP, EDS and FT-IR spectroscopy.

Experimental

Materials

Yttrium(III) nitrate hexahydrate (Y(NO$_3$)$_3$·6H$_2$O, 99.9%), magnesium acetate tetrahydrate (Mg(CH$_3$COO)$_2$·4H$_2$O, 98–102%), citric acid (CA) (C$_6$H$_8$O$_7$ 99.5%) and ethylene glycol (EG) were purchased from the Sigma Aldrich company and have used without purification.

Nanocomposite Synthesis

In a typical experiment, 0.051 mol Y (NO$_3$)$_3$·6H$_2$O and 0.102 Mg (CH$_3$COO)$_2$·4H$_2$O were added to a beaker containing 100 ml of distilled, deionized water, and then, according to Table 1, CA and EG were added to the solution. This solution, stirring at 50 °C for 20 min until a clear solution was obtained. Then, for removing excess water, the solution was heated at 90–100 °C, so it became more and more viscous, which at this stage the complexion between CA and metal ions was carried out. To forming gel, the solution was heated at 140–150 °C for 1 h. At this stage the esterification of CA and EG was occurring (Fig. 1). For complete drying, the gel was placed in an oven at 220 °C for 5 h, to obtain, created a voluminous, brown porous foam. Finally, in the furnace, the brown porous foam was calcined at 800 °C (heating rate 10 °C/min) for 2 h, and then cooled to reach room temperature. Figure 2 summarizes the schematic experimental process.

Characterization Equipment

Thermal decomposition of MgO–Y$_2$O$_3$ composite nanopowder was followed by thermogravimetric analysis (TG-DSC; Model STA 409 PC Luxx, Netzsch, Selb,

Table 1 Experimental parameters and results for various MgO–Y$_2$O$_3$ solutions

Sample no.	CA:TM	CA/ EG	pH	Crystallite size (nm)		Specific surface area (m^2/g)	Average particle size (nm)
				MgO	Y$_2$O$_3$		
S1 102	1:1	3:1	2	10.5	11.3	12.8	22.1
S2 107	1:1	3:1	7	12.3	13.2	10.9	25.1
S3 112	1:1	3:1	12	15.2	16.1	9.8	28.6
S4 502	1:5	3:1	2	9.2	10.1	25.8	21.2
S5 507	1:5	3:1	7	11.3	12.1	20.6	23.3
S6 512	1:5	3:1	12	13.2	13.2	15.8	25.8
S7 1002	1:10	3:1	2	8.7	9.2	52.2	19.5
S8 1007	1:10	3:1	7	10.6	11.1	45.3	28.5
S9 1012	1:10	3:1	12	12.8	13.5	38.9	30.9

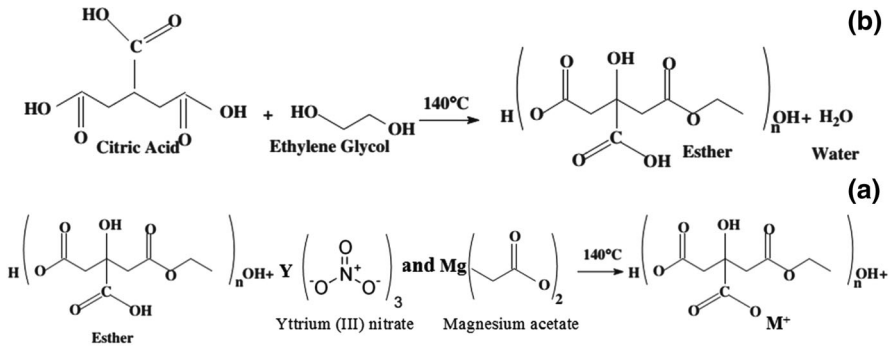Fig. 1 a The schematically for esterification of citric acid with ethylene glycol and b diagram of reaction mechanism of chelation of the Mg acetate and Y nitrate by the polymer
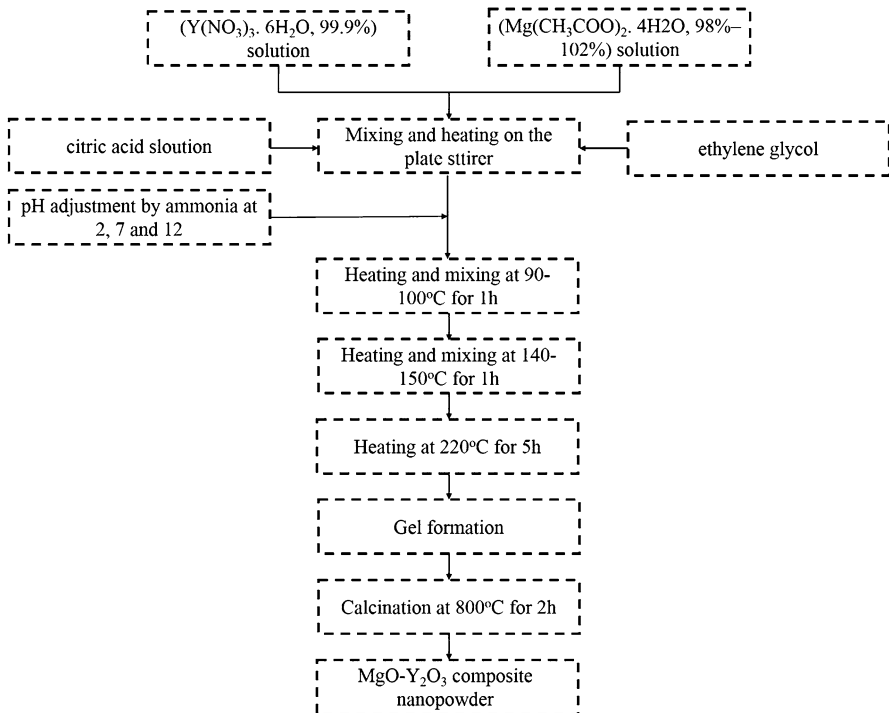

Fig. 2 Schematically of synthesis of MgO–Y_2O_3 nanocomposite Pechini sol–gel method

Germany). For each run, about 15 mg of dried precursor gel was placed in an Al pan. The thermal analyses were performed from room temperature to 1000 °C at a rate of 10 °C/min. The microstructural morphologies and phase distributions of MgO–Y_2O_3 composite nanopowder was studied using field emission scanning electron microscopy (TESCAN, FESEM-MIRA3, Czech Republic, HV: 15 kV) and transmission electron microscopy (TEM Philips CM30 with an accelerating voltage

of 150 kV), the histogram of particle size was obtained from measurements of 150–200 particles in FESEM images. The crystallization of the amorphous precipitate of MgO–Y$_2$O$_3$ composite nanopowder was investigated by XRD using CuKα radiation in a high-resolution powder diffract meter (X'Pert Pro, Philips, Holland). The XRD spectra were acquired by scanning repeatedly over the angular range 2θ = 10°–80° at a scan speed of 5°/min. The crystallite size was calculated by the Rietveld and Popa LB method using MAUD software. Furthermore with this software the degree of crystallization was calculated. The specific surface area of MgO–Y$_2$O$_3$ composite nanopowder was performed using a gas sorption analyzer (Sorptometer Kelvin 1042, Italy), based on the Brunauer–Emmett–Teller (BET) method. For investigation the functional groups of organic material, was studied using Fourier-transform infrared spectrometry (FT-IR spectroscopy; Model JASCO 680—PLUS, Shimadzu, Japan in the region of 400–4000 cm^{-1} using KBr pellets) was used.

Results and Discussion

XRD Results

In this study, have been investigated simultaneously the effect of citric acid to precursors mole ratio and the effect of pH value on the properties of MgO–Y$_2$O$_3$ composite nanopowders. In the fabrication process, the precursor solution was heated to 800 °C with a heating rate of 10 °C/min and held for 2 h before cooling down. Figure 3 shows the XRD patterns of Y$_2$O$_3$–MgO composite nanopowders synthesized according to Table 1, obviously, the synthesized composite
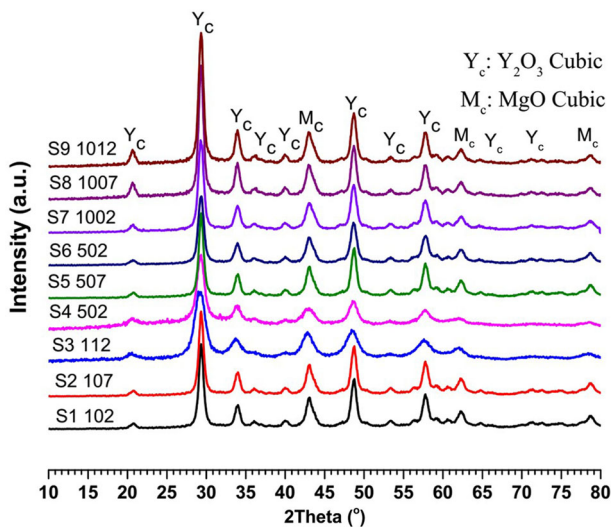

Fig. 3 The XRD patterns of the Y$_2$O$_3$–MgO composite nanopowders synthesized from the precursor solutions according to the Table 1

nanopowders are composed of cubic Y_2O_3 and MgO phases. The average crystallite sizes for these two phases were obtained from the XRD data. According to Table 1, with the increasing CA to TM mole ratio, crystallite size was reduced. Also, by increasing the pH value from 2 to 12 the crystallite size was increased.

FESEM Results

The FESEM image of nanopowders synthesized according to Table 1, are shown in Fig. 4. By increasing the CA to TM mole ratio, the particle size was reduced. Thus, when the CA mole ratio increases, the high amount of –COOH, resulted in a high amount of CA-TM complex. This was caused lower amounts of free Mg^{2+} and Y^{3+} in the solution were existed. So increasing the CA mole ratio reduces the particle size. The distributions for the particles obtained from FESEM images are shown in Fig. 5. When the CA: TM mole ratio was 1:10, the particle sizes are almost 19 nm, then the particle size of the composite nanopowder increases as the pH value
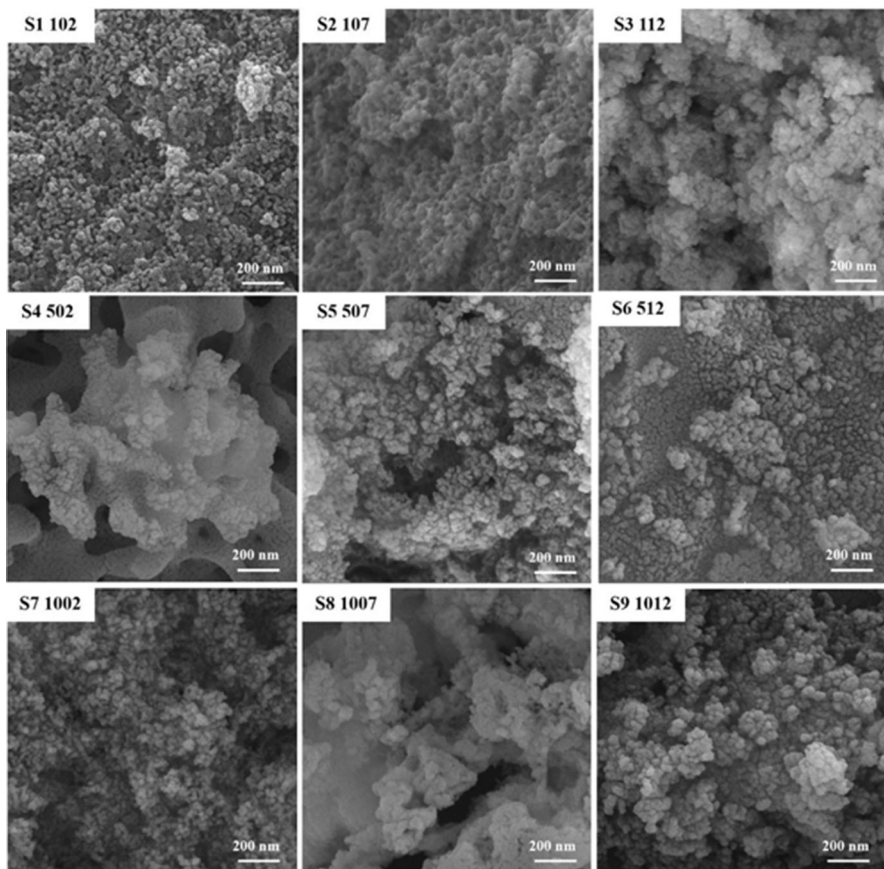

Fig. 4 The FESEM images of Y_2O_3–MgO composite nanopowders synthesized from the precursor solutions according to the Table 1
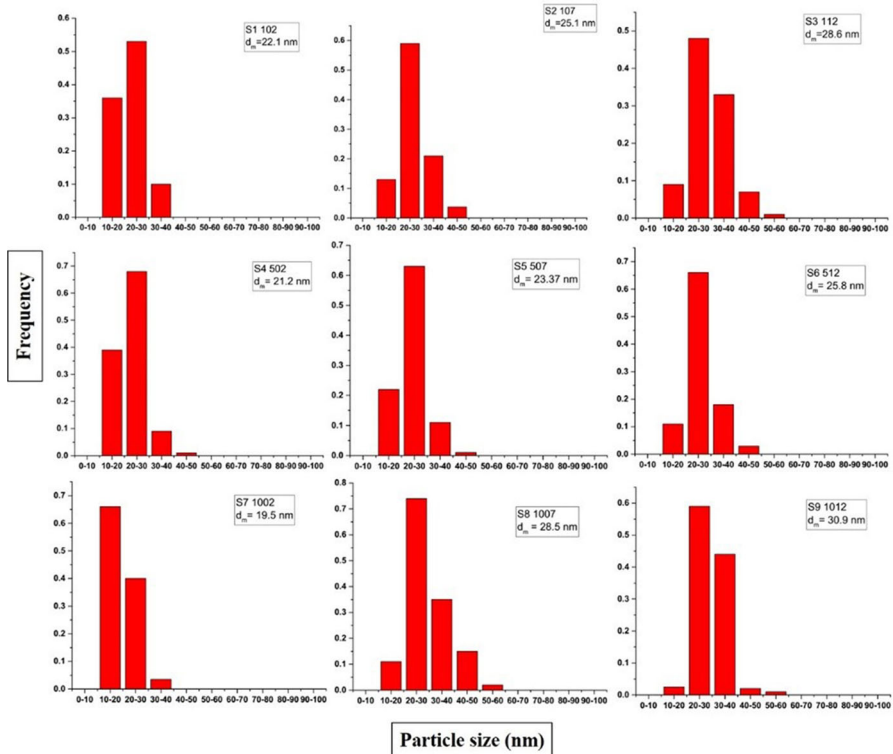
Fig. 5 Particle size distributions for the nanopowders synthesized from the precursor according to the Table 1, In each case, measurements of 100–150 particles were obtained from FESEM images and mean particle diameter, d_m, was indicated

increases from 2 to 12. It should be pointed out that, esterification between CA and EG and the complexion of Mg^{2+} and Y^{3+} in CA solution are dependent on pH. The major effect of pH on the Pechini method was harming esterification between citric acid and ethylene glycol [25]. The reason for particle size growth in alkaline pH can be attributed to the less polyester (gel medium) molecules were formed at high value of pH. It is well known polyester formation (CA-EG reaction) was accelerated at acidic medium. Thus, the lower particle size was observed for the sample S1, S4 and S7 (pH 2) in Table 2. The particle size obtained from FESEM images are shown in Table 2. As seen in Table 1, the particle size was increased with increasing the

Calcination temperatures (°C)	Crystallite size (nm)	
	MgO	Y$_2$O$_3$
600	5.82	5.25
800	10.37	11.91
1000	16	16.88

Table 2 Effect of calcination temperatures on the crystallite size

pH value from 2 to 12. It is noteworthy that the average particle size of the nanopowder S4 502 and S7 1002 is nearly the same, but the specific surface area corresponding to S7 1002 is higher.

For description the distribution of MgO and Y_2O_3 phases, the samples were consolidated by cold pressing and then sintered at 1000 °C for 2 h. BSE FESEM images of the synthesized powders according to Table 1, are shown in Fig. 6. According to FESEM image, bright particle is Y_2O_3 and dark particle is MgO. Thus, the Y-rich particles in the sample produced from the pH 7 and 12. Also, the interconnected disorder particles yttria observed in the powder samples produced from the pH 7 and 12 that can be said this particles are domain phases. According to Fig. 6 (S3, S6 and S9), it was observed that at alkali pH (pH 12), the particle size increased from 28–30 nm to 0.8–1.5 μm. As mentioned before, at alkali pH less polymer was formed and thus the cations (Y^{3+} and Mg^{2+}), was not distribution and
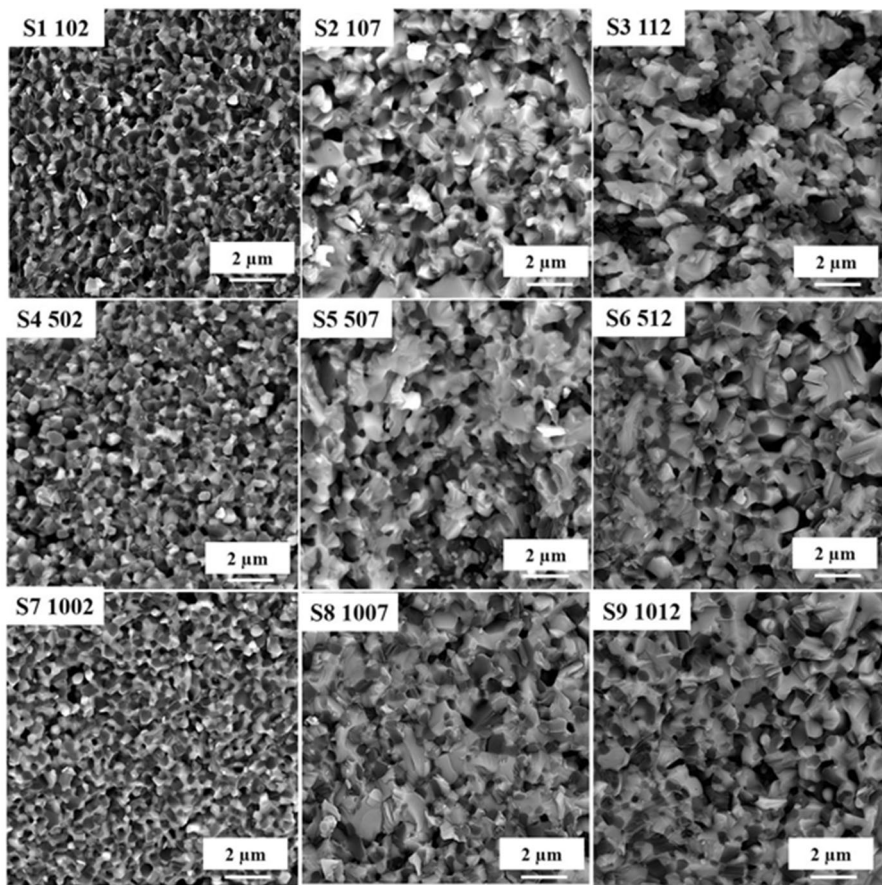

Fig. 6 Backscattered electron FESEM of the fracture surfaces of MgO–Y_2O_3 nanocomposite calcined at 800 °C for 2 h and sintered at 1200 °C for 2 h, and the nanopowders synthesized from the precursor according to the Table 1

coordinated well in the gel medium. So, after the consolidation of nanopowders, MgO could not prevent Y$_2$O$_3$ particle to be growing. As can be seen in Fig. 6, the powder samples produced from the pH 2, MgO and Y$_2$O$_3$ have a uniform distribution phases and average particle size of MgO and Y$_2$O$_3$ are 492 and 441 nm, respectively. As can be seen in Fig. 6, Y$_2$O$_3$ particle size is smaller than the MgO one. So, we can conclude, MgO has prevented the grain growth of Y$_2$O$_3$. Also, completely impressive, the phase boundary between Y$_2$O$_3$ and MgO. The effect of the phase distribution is more than grain size on the optical properties [26].

Characterization of the Optimized Sample

According to XRD, FESEM, and BET results, the optimum sample was synthesized with CA:TM 10:1 and pH 2 (S7 1002) had the average particle size of 19.5 with the spherical morphology, specific surface area 52.2 m^2/g, and uniform distribution of MgO and Y$_2$O$_3$ phases.

TG–DTA Analysis

The thermal characteristics of the gel during the nanopowder synthesis were investigated using the thermal analysis technique. Firstly, the solution prepared with CA:TM 10:1 and pH 2 (S7 1002) was placed in an oven preheated to 250 °C and held for 5 h, during this process, the physical water was released and the nitrates decomposed to form the porous organic foam. Then, the thermal characteristics of
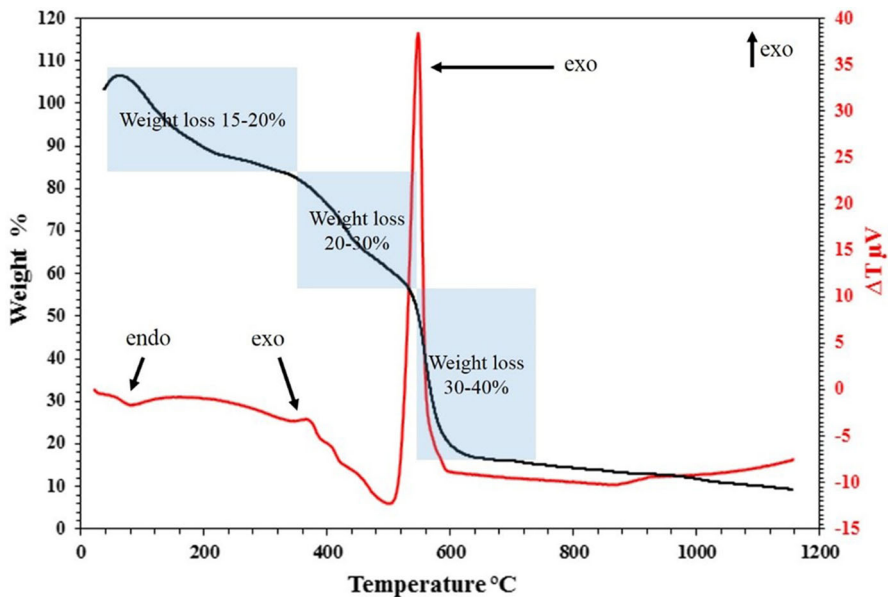

Fig. 7 Plot of differential thermal analysis and thermogravimetry date obtained at a heating rate of 10 °C/min from the organic foam prepared with CA:TM = 10:1

the organic foam were analyzed using a combined TG-DSC setup. The S7 1002 sample was heated from 25 to 1200 °C at the rate of 10 °C/min in flowing air. Figure 7 shows the TG–DTA curves of the precursor. As we can see that three weight-loss steps occur in the TG curve. It was observed on the TG curve that, the first weight loss step over the temperature ranging from the room temperature to about 300 °C with a weight loss of about 15–20% is attributed to adsorbed water molecules which formed during the esterification process. The second weight drop of about 20–30%, from about 450 °C could be due to the oxidation or combustion of the polymer-TM complex and the release of N_xO_y, CO, and CO_2 gases [27]. In the following, in the TG curve, the third weight loss around 550–600 °C had an initial mass loss of 30–40% and it could be attributed to the crystallization. In addition, for temperatures higher than 800 °C no significant weight loss was observed. The endothermic peak in the DTA curve (around 100 °C) is assigned to the vaporing of physical water in the organic foam during heating. The exothermic peak around 400 °C is ascribed to the decomposition of excess CA and NO_3 in the polymeric network and the exothermic peak around 600 °C is ascribed to the crystallization of the residual amorphous phase and forming of metal oxides.

FT-IR Analysis

The FTIR spectra of the organic foam of S71002 and the calcined powder at different temperatures in the wave number range between 400 and 4000 cm^{-1} are illustrated in Fig. 8. The broad absorption band at about 3407 cm^{-1} is assigned to O–H stretching of absorbed water. The bands at 2924 and 2903 cm^{-1} in gel was related to asymmetric and symmetric stretching of –CH_2 respectively [28]. In
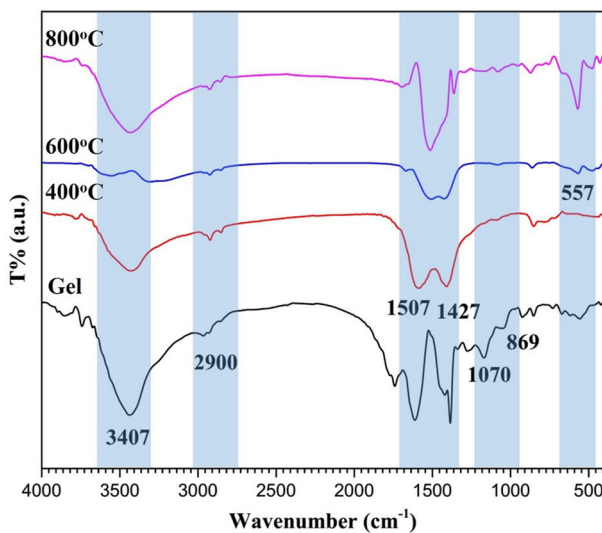

Fig. 8 The FTIR spectra of the organic foam and the nanopowders calcinated at different temperatures (Gel, 400, 600 and 800 °C)

addition, the absorption bands at about 1657 and 1377 cm^{-1} can be related to the asymmetrical and symmetrical stretching of –COO groups while other bands at about 1070 and 869 cm^{-1} are assigned to the v_1 and v_2 modes of the carbonate ions, respectively [29, 30]. Also, the peaks that observed at around 1427–1507 cm^{-1} can be related to the asymmetrical and symmetric stretching vibrations of COO$^-$, respectively; which can be considered as a result to formation of citric acid complexes with Y^{3+} and Mg^{2+} cations [31, 33]. For the nanopowders calcined at higher than 600 °C, the peaks observed at below 557 cm^{-1} are ascribed metal–oxygen stretching vibrations of the composite nanopowder. With increasing the calcination temperature the absorption organic peaks became weaker while absorption peaks of metal–oxygen turn out to be stronger. The FTIR results, is a good match with the TG–DTA results.

XRD Analysis

The XRD patterns of the nanopowders calcined at various temperatures for 2 h are shown in Fig. 9. It is obvious that the crystallinity of the product increases with increasing the calcination temperature. X-ray diffraction pattern of the sample calcined at 400 °C shows that the precursors gel is amorphous. At 600 °C, the strongest characteristic peaks of Y$_2$O$_3$ and MgO with cubic phase were appeared. XRD analysis shows that the precursor transforms completely to the Y$_2$O$_3$ and MgO with cubic phase at around 600 °C. This result is in good agreement with thermal analysis and IR analysis. The influence of the calcination temperatures on the crystallite size is shown in Table 2. The crystallite size of MgO phase increases from 5.82 to 16 nm when the calcination temperature is raised from 600 to 1000 °C.
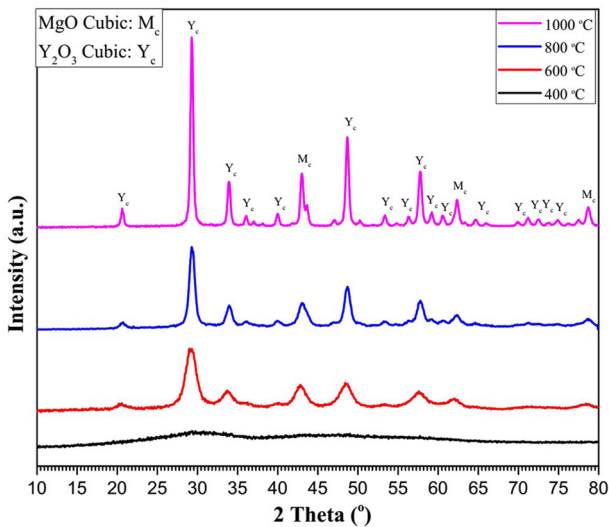

Fig. 9 The XRD patterns of the nanopowders calcinated at different temperatures

FESEM Analysis

In Fig. 10, FESEM photographs of the MgO–Y_2O_3 nanocomposite calcined at 600, 800 and 1000 °C are shown and the size distributions of the particles obtained from FESEM images are shown in Fig. 11. The particle size increases from 15.60 to 34.67 nm when the calcination temperature is raised from 600 to 1000 °C. The average particle size increases with the increase of calcination temperature, and the particle size becomes widely distributed with the increase of calcination temperature. The FESEM results, has a good match with the crystallite size obtained with XRD analysis.
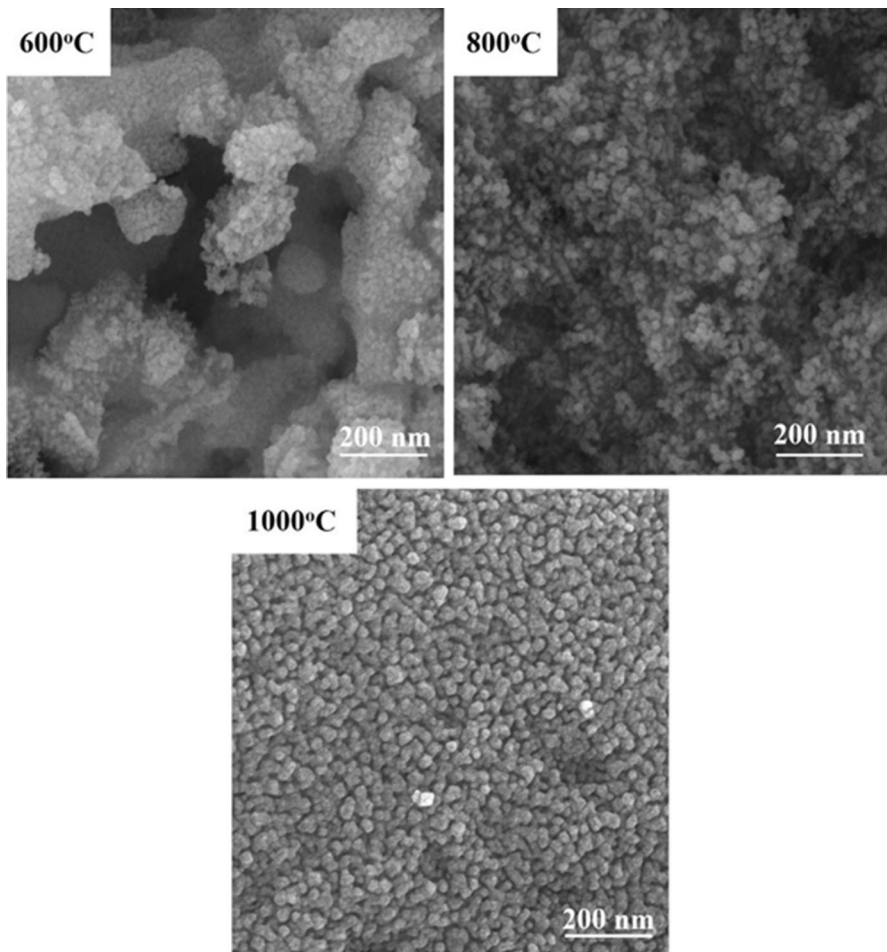

Fig. 10 The FESEM images of Y_2O_3–MgO nanopowders calcinated at different temperatures (600, 800 and 1000 °C)
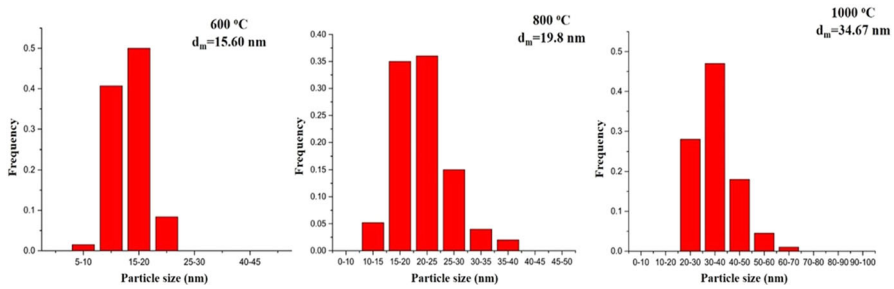
Fig. 11 Particle size distributions for the nanopowders synthesized with different holding temperatures, (600, 800 and 1000 °C). In each case, measurements of 150–200 particles were obtained from FESEM images and mean particle diameter, d_m, was indicated

BET Analysis

In Table 3, the results of particle size measurements of the MgO–Y$_2$O$_3$ nanopowders calcined at 600, 800 and 1000 °C are summarized. The crystallite size obtained by the XRD patterns was defined as d_{XRD}. The average particle size estimated from FESEM images was denoted as d_m. The particle size d_{BET} was calculated from the relation $d_{BET} = 6/\rho \, S_{BET}$, where ρ (3.62 g/cm^3) was the theoretical density of MgO–Y$_2$O$_3$ nanocomposite and S_{BET} was the specific surface area (m^2/g) determined by BET measurement. The d_m, d_{BET} and d_{XRD} were increased with increasing the calcination temperature (d_m: from 15.60 to 34.67 nm, d_{BET}: from 16.33 to 66.66 nm, d_{XRD}: from 5.53 to 16.44 nm). According to the d_m and d_{XRD}, the powder calcined at 600 °C, it could be concluded that each particle shown in the FESEM images included three crystallites. The d_{BET} powder of that calcined at 600 °C was nearly the same as the average particle size (d_m) obtained from FESEM images. In contrast, the powder calcined at 800 and 1000 °C showed a large difference between d_m and d_{BET}. Finally, it can be concluded that if d_{BET} is lower than d_m, it implies that nitrogen gas used for BET measurement cannot completely cover the particle surfaces; so it can be said that the powder has been agglomerated. With this interpretation, the powder was calcined at 600 °C, with low agglomeration. To investigate the agglomeration, agglomeration factor (AF) can be defined. Here, if AF value is closer to 1, the amount of agglomeration is lower.

Table 3 Effect of calcination temperatures on the d_{XRD}, d_m and d_{BET} of MgO–Y$_2$O$_3$ nanopowder (MY4)

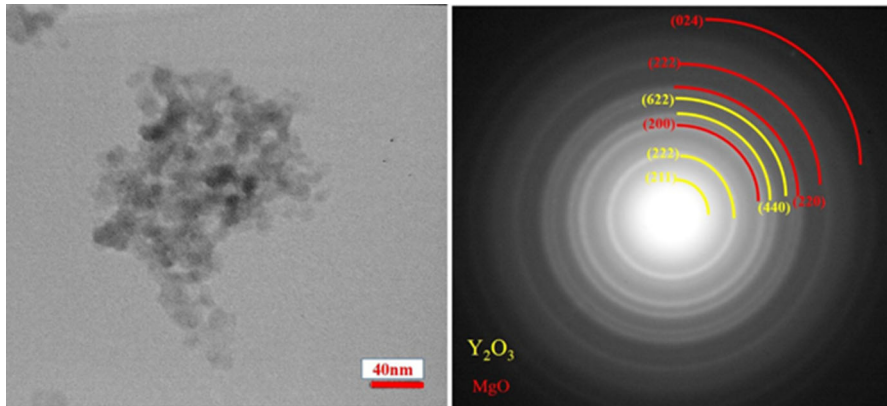| Calcination temperatures (°C)	d_{XRD} (nm) (average crystallite size between MgO and Y$_2$O$_3$ phase)	S_{BET} (m^2/g)	d_{BET} (nm)	d_m (nm)	Agglomeration factor (AF) d_m/d_{BET}
600	5.53	101.96	16.33	15.60	0.95
800	11.14	52.20	32.05	19.80	0.61
1000	16.44	25.83	66.66	34.67	0.52

Fig. 12 The TEM photograph and selected area diffraction patterns of the MgO–Y_2O_3 nanopowder calcined at 600 °C for 2 h
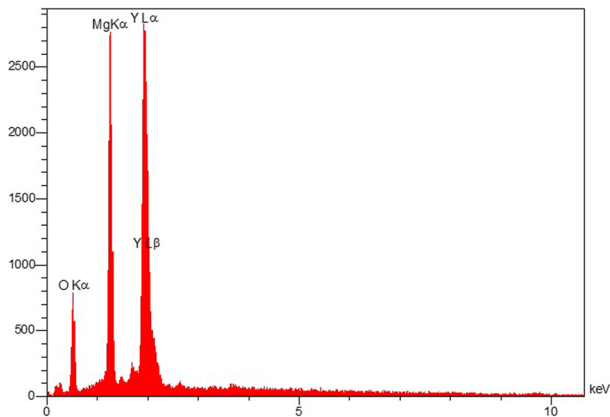

Fig. 13 The EDS spectra acquired of the MgO–Y_2O_3 nanopowder calcined at 600 °C for 2 h

TEM Analysis

Furthermore, decomposition of MgO–Y_2O_3 ester via hydrogen carbonate to MgO–Y_2O_3 at temperatures, upper than 600 °C could be easily concluded from FT-IR. Meanwhile, the XRD patterns revealed that the precursor (MgO–Y_2O_3 gel) transformed completely to the cubic MgO–Y_2O_3 at 600 °C. The Transmission electron microscopy (TEM) image with selected area diffraction patterns of MgO–Y_2O_3 nanopowder calcined at 600 °C for 2 h are shown in Fig. 12. According to the TEM images, particles have spherical morphology. Also, the particle size is about 10–15 nm in diameter. So, the particle size obtained with TEM images has good match with a particle size of FESEM images. According to Fig. 12b, the characteristic pattern of (200), (220), and (024) of MgO and (211), (222), (440), and (622) of yttria was clearly observed. Here, the results of selected area diffraction

Table 4 ICP analysis results of non-rare earth impurities in sol–gel-synthesized MgO–Y$_2$O$_3$ nanpowder

Non-rare earth impurities	Content (ppm)
Ag	3.8
Be	3.3
La	7
Li	5
Fe	8
Pb	2.5

patterns, was good agreement with Chun-Hu Chen coworker [32]. According to the d_m and d_{XRD}, the powder calcined at 600 °C, can be concluded that, each particle shown in the FESEM images include three crystallites.

The EDS spectra for MgO–Y$_2$O$_3$ composite nanopowder (S7 1002, calcined at 600 °C for 2 h) are shown in Fig. 13. The semi quantitative EDS investigates exhibited that matrix mainly contains yttrium, oxygen, and magnesium elements. Furthermore, Table 4 displays ICP elemental analysis for main non-rare earth impurities of the MgO–Y2O3 composite nanopowder used as initial material which is of high purity (over 99.99%) in the investigative work.

Conclusion

We have synthesized Y$_2$O$_3$–MgO nanocomposite powders by Pechini method. The pH value of the starting solution plays an important role in controlling particle size and phase distribution. According to results by increasing the mole ratio of CA to TM, the average particle size of MgO–Y$_2$O$_3$ composite nanopowder has reduced and by increasing the pH from 1 to 12, the particle size and the specific surface area of MgO–Y$_2$O$_3$ composite nanopowder has increased. Also, a change in the pH can affect both the chemical reactivity of CA and EG molecules and the structure of the Y$_2$O$_3$–MgO nanocomposite polymeric network. The major effect of alkali pH value of the Pechini method is that it can destroy esterification between citric acid and ethylene glycol, thereby less polymeric medium was existed for good distribution of Mg^{2+} and Y^{3+} cations in the gel. The optimum sample was prepared with CA:TM equal to 10:1, pH 2 and calcined at 600 °C for 2 h, have an average particle size of 10–15 nm.

References

1. B. H. Kear, R. Sadangi, V. Shukla, T. Stefanik, and R. Gentilman. Submicron-grained transparent yttria composites. In *Proceedings SPIE 5786, Window and Dome Technologies and Materials IX*, p. 227 (2005).
2. M. Ahsanzadeh-Vadeqani, R. S. Razavi, M. Barekat, G. H. Borhani, and A. K. Mishra (2016). Preparation of yttria nanopowders for use in transparent ceramics by dry ball-milling technique. *J. Eur. Ceram. Soc.* doi:10.1016/j.jeurceramsoc.2016.12.006.

3. R. Marder, R. Chaim, G. Chevallier, and C. Estournès (2011). Effect of 1 wt% LiF additive on the densification of nanocrystalline Y_2O_3 ceramics by spark plasma sintering. *J. Eur. Ceram. Soc.* **31**, 1057–1066.

4. R. Marder, R. Chaim, G. Chevallier, and C. Estournes (2011). Densification and polymorphic transition of multiphase Y_2O_3 nanoparticles during spark plasma sintering. *Mater. Sci. Eng. A* **528**, 7200–7206.

5. X. Gang, Y. Shanjiang, Y. Xujie, L. Lude, and W. Xin (1998). Preparation and characterization of nanocrystals Y_2O_3. *J. Funct. Mater.* **29**, 92–95.

6. L. Jin, G. Zhou, S. Shimai, J. Zhang, and S. Wang (2010). ZrO_2-doped Y_2O_3 transparent ceramics via slip casting and vacuum sintering. *J. Eur. Ceram. Soc.* **30**, 2139–2143.

7. D. C. Harris (1998). Durable 3–5 μm transmitting infrared window materials. *Infrared Phys. Technol.* **39**, 185–201.

8. T. Stefanik, R. Gentilman, and P. Hogan. Nanocomposite optical ceramics for infrared. In *Proceedings of SPIE 6545, Window and Dome Technologies and Materials X*, p. 65450A (2007).

9. Y. Huang, D. Jiang, J. Zhang, Q. Lin, and Z. Huang (2010). Sintering of transparent yttria ceramics in oxygen atmosphere. *J. Am. Ceram. Soc.* **93**, 2964–2967.

10. Q. Zhu, A. R. Oganov, and A. O. Lyakhov (2013). Novel stable compounds in the MgO system under high pressure. *Phys. Chem. Chem. Phys.* **15**, 7696–7700.

11. P. A. Tellex and J. R. Waldron (1955). Reflectance of magnesium oxide. *JOSA* **45**, 19.

12. S. F. Wang, J. Zhang, D. W. Luo, F. Gu, D. Y. Tang, Z. L. Dong, G. E. B. Tan, W. X. Que, T. S. Zhang, S. Li, et al. (2013). Transparent ceramics: processing, materials and applications. *Prog. Solid State Chem.* **41**, 20–54.

13. M. Ghaderi, R. S. Razavi, M. R. Loghman-Estarki, and S. Ghorbani (2016). Spark plasma sintering of transparent Y_2O_3 ceramic using hydrothermal synthesized nanopowders. *Ceram. Int.* **42**, 14403–14410.

14. M. R. Loghman-Estarki, F. Davar, S. Ghorbani, M. Zendehdel, and M. H. Taherian (2016). Synthesis and characterization of aluminum oxy nitride (AlON) from the nanosized gel precursor. *Ceram. Int.* **42**, 16861–16866.

15. R. S. Razavi, M. Ahsanzadeh-Vadeqani, M. Barekat, M. Naderi, S. H. Hashemi, and A. K. Mishra (2016). Effect of sintering temperature on microstructural and optical properties of transparent yttria ceramics fabricated by spark plasma sintering. *Ceram. Int.* **42**, 7819–7823.

16. M. Hajizadeh-Oghaz, R. S. Razavi, and A. Ghasemi (2015). Synthesis and characterization of ceria–yttria co-stabilized zirconia (CYSZ) nanoparticles by sol–gel process for thermal barrier coatings (TBCs) applications. *J. Sol-Gel Sci. Technol.* **74**, 603–612.

17. T.-T. Fang and J.-D. Tsay (2001). Effect of pH on the chemistry of the barium titanium citrate gel and its thermal decomposition behavior. *J. Am. Ceram. Soc.* **84**, 2475–2478.

18. H.-F. Yu and K.-C. Huang (2003). Effects of pH and citric acid contents on characteristics of ester-derived BaFe 12 O 19 powder. *J. Magn. Magn. Mater.* **260**, 455–461.

19. B. D. Cullity and J. W. Weymouth (1957). Elements of X-ray diffraction. *Am. J. Phys.* **25**, 394–395.

20. M. Pudukudy and Z. Yaakob (2014). Catalytic aspects of ceria–zirconia solid solution: Part-I an update in the synthesis, properties and chemical reactions of ceria zirconia solid solution. *Pharma Chem.* **6**, 188.

21. S. Sakka. *Handbook of Sol-Gel Science and Technology. Sol-Gel Processing*, vol. 1 (Springer, Berlin, 2005).

22. M. R. Loghman-Estarki, M. Hajizadeh-Oghaz, H. Edris, and R. S. Razavi (2013). Comparative studies on synthesis of nanocrystalline Sc_2O_3–Y_2O_3 doped zirconia (SYDZ) and YSZ solid solution via modified and classic Pechini method. *CrystEngComm* **15**, 5898–5909.

23. M. H. Oghaz, R. S. Razavi, M. R. Loghman-Estark, and R. Ghasemi (2012). Optimization of morphology and particle size of modified sol gel synthesized YSZ nanopowder using Taguchi method. *J. Nano Res.* **21**, 65–70.

24. M. Hajizadeh-Oghaz, R. S. Razavi, and M. Khajelakzay (2015). Optimizing sol–gel synthesis of magnesia-stabilized zirconia (MSZ) nanoparticles using Taguchi robust design for thermal barrier coatings (TBCs) applications. *J. Sol-Gel Sci. Technol.* **73**, 227–241.

25. G. Di Girolamo, C. Blasi, M. Schioppa, and L. Tapfer (2010). Structure and thermal properties of heat treated plasma sprayed ceria–yttria co-stabilized zirconia coatings. *Ceram. Int.* **36**, 961–968.

26. L. L. Beecroft and C. K. Ober (1997). Nanocomposite materials for optical applications. *Chem. Mater.* **9**, 1302–1317.

27. S. Xu, J. Li, H. Kou, Y. Shi, Y. Pan, and J. Guo (2015). Spark plasma sintering of Y$_2$O$_3$–MgO composite nanopowder synthesized by the esterification sol–gel route. *Ceram. Int.* **41**, 3312–3317.

28. S. Shirinparvar, R. S. Razavi, F. Davar, M. R. Loghman-Estarki, M. Hajizadeh-Oghaz, and S. Ghorbani (2016). Synthesis, characterization and optical properties of Zr^{+4}/La^{+3}/Nd^{+3} tri-doped yttria nanopowder by sol–gel combustion method. *Ceram. Int.* **42**, 10551–10558.

29. M. Ahsanzadeh-Vadeqani, and R. S. Razavi (2016). Spark plasma sintering of zirconia-doped yttria ceramic and evaluation of the microstructure and optical properties. *Ceram. Int.* **42**, 18931–18936.

30. S. G. Cho, P. F. Johnson, and R. A. Condrate Sr. (1990). Thermal decomposition of (Sr, Ti) organic precursors during the Pechini process. *J. Mater. Sci.* **25**, 4738–4744.

31. S. Wang, C. An, Y. Zhang, Z. Zhang, and Y. Qian (2006). Ethanothermal reduction to MoO$_2$ microspheres via modified Pechini method. *J. Cryst. Growth* **293**, 209–215.

32. C.-H. Chen, J. K. M. Garofano, C. K. Muoto, A. L. Mercado, S. L. Suib, M. Aindow, M. Gell, and E. H. Jordan (2011). A foaming esterification sol–gel route for the synthesis of magnesia–yttria nanocomposites. *J. Am. Ceram. Soc.* **94**, 367–371.

33. S. Xu, J. Li, C. Li, Y. Pan, and J. Guo (2015). Hot pressing of infrared-transparent Y$_2$O$_3$–MgO nanocomposites using sol–gel combustion synthesized powders. *J. Am. Ceram. Soc.* **98**, 1019–1026.

34. S. Ghorbani, R. S. Razavi, M. R. Loghman-Estarki, and A. Alhaji (2016). Synthesis of MgO–Y$_2$O$_3$ composite nanopowder with a high specific surface area by the Pechini method. *Ceram. Int.* **43**, 345–354.